

NASA/CR-1999-209355
ICASE Report No. 99-25



Solving Upwind-biased Discretizations II: Multigrid Solver Using Semicoarsening

Boris Diskin
ICASE, Hampton, Virginia

Institute for Computer Applications in Science and Engineering
NASA Langley Research Center
Hampton, VA

Operated by Universities Space Research Association



National Aeronautics and
Space Administration

Langley Research Center
Hampton, Virginia 23681-2199

Prepared for Langley Research Center
under Contract NAS1-97046

July 1999

SOLVING UPWIND-BIASED DISCRETIZATIONS II: MULTIGRID SOLVER USING SEMICOARSENING

BORIS DISKIN*

Abstract. This paper studies a novel multigrid approach to the solution for a second order upwind-biased discretization of the convection equation in two dimensions. This approach is based on semicoarsening and well balanced explicit correction terms added to coarse-grid operators to maintain on coarse grids the same cross-characteristic interaction as on the target (fine) grid. Colored relaxation schemes are used on all the levels allowing a very efficient parallel implementation. The results of the numerical tests can be summarized as follows:

1. The residual asymptotic convergence rate of the proposed $V(0,2)$ multigrid cycle is about 3 per cycle. This convergence rate far surpasses the theoretical limit $(4/3)$ predicted for standard multigrid algorithms using full coarsening. The reported efficiency does not deteriorate with increasing the cycle depth (number of levels) and/or refining the target-grid mesh spacing.
2. The full multigrid algorithm (FMG) with two $V(0,2)$ cycles on the target grid and just one $V(0,2)$ cycle on all the coarse grids always provides an approximate solution with the algebraic error less than the discretization error. Estimates of the total work in the FMG algorithm are ranged between 18 and 30 minimal work units (depending on the target discretization). Thus, the overall efficiency of the FMG solver closely approaches (if does not achieve) the goal of the textbook multigrid efficiency.
3. A novel approach to deriving a discrete solution approximating the true continuous solution with a relative accuracy given in advance is developed. An adaptive multigrid algorithm (AMA) using comparison of the solutions on two successive target grids to estimate the accuracy of the current target-grid solution is defined. A desired relative accuracy is accepted as an input parameter. The final target grid on which this accuracy can be achieved is chosen automatically in the solution process. The actual relative accuracy of the discrete solution approximation obtained by AMA is always better than the required accuracy; the computational complexity of the AMA algorithm is (nearly) optimal (comparable with the complexity of the FMG algorithm applied to solve the problem on the optimally spaced target grid).

Key words. convection, upwind-biased discretization, multigrid solvers, textbook multigrid efficiency

Subject classification. Applied and Numerical Mathematics

1. Introduction. Full multigrid (FMG) algorithms are known to be very efficient solvers for complicated systems of partial differential equations. It was rigorously proved (see [3] and [4]) that these algorithms can solve a general discretized elliptic problem to the discretization accuracy in a computational work which is only a small multiple of the operation count in the discrete problem itself. This efficiency is called the textbook multigrid efficiency (TME). The target-grid (grid h) solution obtained by a FMG solver is usually required to satisfy to the following condition: its *algebraic error* $\|u^h - \tilde{u}^h\|$ must be less than the *discretization error* $\|u^h - U^h\|$, where u^h is the exact discrete solution, \tilde{u}^h is the FMG solution, U^h is a reasonable target-

*Institute for Computer Applications in Science and Engineering, Mail Stop 132C, NASA Langley Research Center, Hampton, Virginia 23681-2199 (email: bdiskin@icase.edu). This research was supported by the National Aeronautics and Space Administration under NASA Contract No. NAS1-97046 while the author was in residence at the Institute for Computer Applications in Science and Engineering (ICASE), NASA Langley Research Center, Hampton, Virginia 23681-2199.

grid representation of the true solution of the differentiable equation, and $\|\cdot\|$ is a given norm of interest. Then the *total error* $\|\tilde{u}^h - U^h\|$ is bounded above by sum of the algebraic and discretization errors. In solving nonelliptic problems, regular FMG algorithms sometimes fail to achieve such an accurate solution and then other very work-consuming methods are applied (either instead of or in addition to a FMG algorithm) to solve the problems.

The goal of achieving TME in solving complicated computational fluid dynamics (CFD) problems attracts recently many researchers (see, e.g., the list of references in [5]). Many of textbook efficient multigrid CFD solvers developed in the last decade are based on the idea of separation of the elliptic and nonelliptic factors contributing to the corresponding system of partial differential equations. (See [9], [14], [15], [17], [18].) In all these solvers, the nonelliptic part was represented by the advection operator.

The simplest way to solve the advection operator is to employ the downstream marching. If the corresponding discretization is a stable upwind discretization and the field of velocities does not recirculate, then this marching proves to be a very efficient solver yielding an accurate solution to a *nonlinear* advection equation in just a few sweeps (a single downstream sweep provides the exact solution to a linearized problem). However, if a discretization of the advection operator is not fully upwind (e.g., only upwind biased) the marching in its pure form is inapplicable. Other single-grid methods like defect-correction iterations or predictor-corrector technique can be used instead. In the recent paper [12], we showed that the number of defect-correction sweeps required to derive an accurate solution to the target discrete problem may be grid dependent. For example, in problems where the target operator is second order accurate while the correction is computed in solving a first order accurate discretization, the necessary number of iterations grows on fine grids approximately as $h^{-1/3}$, where h is the grid meshsize. A detailed analysis of the predictor-corrector scheme is the subject of future studies. In many practical cases, these single-grid methods may result in very efficient solvers. However, each of them implements, one way or another, the idea of marching. In other words, their efficiency is significantly based on the correctness of the order in which values at grid nodes are updated. The consequent order of grid passages seems to be a serious obstacle for transferring these algorithms on parallel computers. In this paper, we suggest a novel multigrid solver to the advection equation employing colored relaxation schemes on all the levels. Coloring implies that discrete equations at grid nodes of the same color can be relaxed simultaneously (in parallel). Such schemes naturally possess a very high level of parallelism.

It has long been known that standard multigrid solvers to the advection equation employing full coarsening suffer an inherent slowdown in problems where the velocity direction does not coincide with the grid lines (see [1], [2]). This poor convergence is explained by an increased cross-characteristic interaction (e.g., dissipation) on coarse grids. The difficulty associated with the cross-characteristic interaction is very prominent in homogeneous problems with characteristics emanating from the boundary. In these problems, the quality of the coarse-grid approximation is determined by how well certain incoming oscillations are advected from the inflow boundary into the domain. The increased coarse-grid cross-characteristic interaction causes a decay and a phase shift of these incoming oscillations which are significantly different from their values on the fine grid. Following [6], the cure proposed in this paper is to use *semicoarsening* together with a well balanced correction of coarse-grid operators allowing the coarse grids to maintain essentially the same cross-characteristic interaction as on the target (fine) grid. The resulting multigrid cycles demonstrate good asymptotic convergence rates, far overcoming the theoretical limit for full-coarsening algorithms.

The efficiency of the present multigrid algorithm does not deteriorate in multiple iterations, i.e. it demonstrates a good asymptotic convergence rate. Nevertheless, we believe that the role of a fast *asymptotic*

convergence is often overestimated. It is true that in elliptic problems the asymptotic convergence rate is defined by the slowest-to-converge error component and, therefore, a good asymptotic rate implies good convergence throughout the solution process. In solving nonelliptic problems, a fast asymptotic convergence is usually achieved only when all the troubling components have already been carried out of the domain of interest by many (slower) iterations (see, e.g., [10] and [12]). Thus, fast converging iterations usually follow many those with much slower convergence rates. Moreover, in some problems, yielding a very accurate solution does not necessarily require a fast per-cycle convergence. These considerations have brought us to another important issue addressed in this paper which is criteria for stopping further computing when an accurate enough solution is achieved. A widely used criterion is sufficiently small residuals in the corresponding discrete equations. To satisfy this criterion, the algorithm is generally expected to be iterated many times and a good asymptotic convergence is, thus, really important. However, it was realized in many experimental and theoretical works that most of the computational time under this criterion is expended for approximating the discrete solution rather than the true solution of the differential problem. An approximation to the differential solution within the discretization accuracy is reached long before the residuals in the discrete problem are reduced to a desired low level. Moreover, small residuals cannot, actually, ensure a good accuracy as well. In nonelliptic problems, some slow-to-converge error components are quite smooth along characteristics and possibly oscillating in the cross-characteristic direction, therefore, their residuals are very small comparing with other error components of the same amplitude. Thus, small residuals (say, in L_2 norm) does not necessarily imply small amplitudes for these components.

The well-known alternative to the small-residuals stopping criterion is the FMG approach, where the necessary number of iterations on each grid is defined in advance. This approach assumes an a priori choice of a target grid and a discretization on it, and, then, the FMG algorithm provides a target-grid solution approximation with the algebraic error less than the discretization error. This is a good option, especially, when the accuracy of the target-grid discretization and convergence properties of the FMG algorithm for the problem of interest were previously established. In many practical cases, however, where the true solution is unknown, either analytically or from an experience, engineers opt to drive residuals to the machine zero level in order to be sure that at least the discrete problem is solved. Another difficulty associated with both the “regular FMG” and “small residuals” approaches is the need of an off-line analysis in order to establish the accuracy of the obtained solution. In many cases, this analysis indicates that either the desired accuracy has not been achieved because of a bad discretization error on the chosen grid and the problem should be resolved on a finer grid, or the desired accuracy could be reached on a coarser grid in much shorter time. In this paper, we propose another criterion indicating that a solution approximation possessing a desired relative accuracy has been obtained. This criterion is the *comparison of solutions on different grids*. Our experiments with an *adaptive multigrid algorithm* (AMA) using this criterion where the choice of an appropriate final discretization grid is an essential part of the solver are reported in Section 5 (see also [12]).

In Section 2, we formulate the model problem and introduce the main ideas for the multigrid treatment of the cross-characteristic interaction. In the next Section 3, we define and test multigrid cycles which, then, are employed in framework of FMG solvers (Section 4) and AMA solvers (Section 5).

2. Model Problem Description.

2.1. Differential Equation. The model problem we study in this paper is the two-dimensional (2D) constant-coefficient convection equation

$$(2.1) \quad LU \equiv (\bar{a} \cdot \nabla)U = F(x, y),$$

where $\bar{a} = (a_1, a_2)$ is a given vector. The solution $U(x, y)$ is a differentiable function defined on the unit square $(x, y) \in [0, 1] \times [0, 1]$.

Let ϕ be the nonalignment angle (another name which is common in CFD is the angle of attack), i.e., the angle between the vector \bar{a} and the positive direction of the x axis; $t = \tan \phi = a_2/a_1$ is the nonalignment parameter. For simplicity, we assume a horizontal inclination $a_1 \geq a_2 \geq 0$ and, therefore, $1 \geq t \geq 0$. We call the x axis the *reference axis*.

Equation (2.1) can be rewritten as

$$(2.2) \quad \partial_\xi U = f(x, y),$$

where $f(x, y) = F(x, y)/|\bar{a}|$, $|\bar{a}| = \sqrt{a_1^2 + a_2^2}$, and $\xi = \frac{x+ty}{\sqrt{1+t^2}}$ is a variable along the characteristic of (2.1). Equation (2.1) is subject to Dirichlet boundary conditions at the inflow boundary $x = 0$ and periodic conditions in the y direction.

$$(2.3) \quad U(0, y) = g(y), \quad U(x, y) = U(x, y + 1),$$

where $g(y)$ is a given function.

In the 2D constant-coefficient case which is studied in this paper, characteristics of (2.1) are straight lines defined by the velocity direction (*characteristic lines*). A function is called a *characteristic component* if it is much more smooth in the characteristic direction than in other directions. Possible extensions to the three dimensions (3D) and to variable velocity fields are briefly discussed at Section 6.

2.2. Target-Grid Discretization. The approach we follow is to use a fixed Cartesian coordinate system independent of the characteristic direction. The problem (2.2)-(2.3) is discretized on the 2D Cartesian uniform grid with meshsize h in both the x and y directions. The target discretization grid is always assumed to be a uniform (square) grid.

Let u_{i_1, i_2} be a discrete approximation to the solution $U(x, y)$ at the point $(x, y) = (i_1 h, i_2 h)$. To derive a proper discretization, we exploit the idea of a *low-dimensional prototype* introduced in [6]. Briefly, the low-dimensional prototype is a good discretization of the target (nonelliptic) differential problem on the grid induced by intersections of the Cartesian multidimensional discretization grid with the characteristic (low-dimensional) manifold (characteristic line in our case). (See Figure 2.1.) For our studies, we choose the low-dimensional prototype to be the (one-dimensional) second order accurate four-point discretization of the first derivative, corresponding to the Van Leer's scheme with $\kappa = 0$.

$$(2.4) \quad \frac{1}{4h\sqrt{1+t^2}} \left(u_{i_1+1, i_2+t} + 3u_{i_1, i_2} - 5u_{i_1-1, i_2-t} + u_{i_1-2, i_2-2t} \right) = f_{i_1, i_2}.$$

The 2D discretization is obtained from the low-dimensional prototype by replacing function values at the ghost points (points with fractional vertical indexes) by weighted averages of the values at the vertically adjacent genuine grid points. The resulting *narrow* discretization is defined by

$$(2.5) \quad L^h u_{i_1, i_2} \equiv \frac{1}{4\sqrt{1+t^2}h} \left(\begin{aligned} & (1-t) \left(u_{i_1+1, i_2} + 3u_{i_1, i_2} - 5u_{i_1-1, i_2} + u_{i_1-2, i_2} \right) \\ & + t \left(u_{i_1+1, i_2+1} + 3u_{i_1, i_2} - 5u_{i_1-1, i_2-1} + u_{i_1-2, i_2-2} \right) \end{aligned} \right) = f_{i_1, i_2};$$

$$i_1 = 1, 2, \dots, N-1, \quad i_2 = 1, 2, \dots, N, \quad N = 1/h;$$

$$u_{0, i_2} = g(i_2 h), \quad u_{-1, i_2} = g'(i_2 h).$$

The outflow boundary conditions at $i_1 = N$ are discretized by the second order accurate *narrow upwind* scheme.

$$(2.6) \quad L^h u_{N,i_2} \equiv \frac{1}{2\sqrt{1+t^2}h} \left((1-t) \left(3u_{N,i_2} - 4u_{N-1,i_2} + u_{N-2,i_2} \right) + t \left(3u_{N,i_2} - 4u_{N-1,i_2-1} + u_{N-2,i_2-2} \right) \right) = f_{N,i_2}.$$

In numerical experiments reported below, we used a corrected outflow discretization to provide the same cross-characteristic interaction as in the interior of the domain. See details in Sections 2.3 and 2.4. The discretization of the right-hand side function is $f_{i_1,i_2} = F(i_1 h, i_2 h)/|\bar{a}|$. Function $g'(y)$ is an additional numerical boundary condition. In model problems, where the exact solution $U(x, y)$ is known, one can define $g'(y) = U(-h, y)$.

The discrete scheme (2.5) is upwind biased, i.e., not a pure upstream scheme, in the interior since, for defining the operator value at the point (i_1, i_2) , the solution values at the downstream points $(i_1 + 1, i_2)$ and $(i_1 + 1, i_2 + 1)$ are required.

2.3. Cross-Characteristic Interaction. The cross-characteristic interaction introduced by a discrete operator can be quantitatively estimated as the coefficient of the lowest pure cross-characteristic derivative appearing in the first differential approximation (FDA) to the discrete operator (see [19]). The FDA to (2.5) taken for the characteristic component is given by

$$(2.7) \quad FDA(L^h) = \partial_\xi - h^2 \frac{t(1-t)(1-2t)}{12\sqrt{1+t^2}} \partial_{yyy} + h^3 \frac{t(1-t)(1-3t+3t^2)}{8\sqrt{1+t^2}} \partial_{yyy}.$$

We included two (the second and the third order) terms into consideration in order to secure a more generality. Usually, the second order term (related to ∂_{yyy}) determines the main part of the cross-characteristic interaction; at some slopes ($t \approx 0.5$), however, this term degenerates and the following third order term becomes important. Moreover, involving these two terms together makes possible to apply the same arguments to analyzing other (possibly higher order) advection schemes, e.g., Van Leer's schemes corresponding to different κ .

The true measure of the cross-characteristic interaction should be calculated as a coefficient of a derivative with respect to the cross-characteristic variable $\eta = \frac{-tx+y}{\sqrt{1+t^2}}$. In the constant-coefficient narrow-discretization case, however, this coefficient is just proportional to the factor of the corresponding y -derivative. The cross-characteristic interaction induced by the operator itself is referred to as *inherent cross-characteristic interaction*, to distinguish it from the *explicit cross-characteristic interaction* introduced below.

Previous studies on different types of nonelliptic equations (see [1], [6], [9] and [11]) have shown that the main difficulty in constructing an efficient multigrid solver is a poor coarse-grid approximation to the fine-grid characteristic error components. It was observed that a coarse-grid operator defined on a grid built by *full coarsening* (i.e., when all the coarse-grid meshsizes are twice as large as their counterparts of the fine grid) unavoidably introduces a too strong cross-characteristic interaction. On the other hand, a narrow discretization on a semicoarsened grid (only the reference axis meshsize is doubled) results in a coarse-grid cross-characteristic interaction which is weaker than required. However, we can supply this operator on the semicoarsened grid with additional (explicit) terms, so that the *total coarse-grid cross-characteristic interaction* would be exactly the same as on the fine grid.

2.4. Coarse-Grid Discretization. The coarse grids used in this multigrid construction are rectangular grids with fixed (integer) aspect ratios $m = h_x/h_y$, where h_x and h_y are the meshsizes in the x and y axes respectively.

The preliminary (without explicit terms) narrow coarse-grid discretization on the grid with aspect ratio m is derived from the low-dimensional prototype (cf. (2.5) and (2.6)).

$$(2.8) \quad L^{(h_x, h_y)} u_{i_1, i_2} \equiv \frac{1}{4mh_y\sqrt{1+t^2}} \left((1-s) \left(u_{i_1+1, i_2+k} + 3u_{i_1, i_2} - 5u_{i_1-1, i_2-k} + u_{i_1-2, i_2-2k} \right) \right. \\ \left. + s \left(u_{i_1+1, i_2+(k+1)} + 3u_{i_1, i_2} - 5u_{i_1-1, i_2-(k+1)} + u_{i_1-2, i_2-2(k+1)} \right) \right) = f_{i_1, i_2};$$

$$(2.9) \quad L^{(h_x, h_y)} u_{M, i_2} \equiv \frac{1}{2mh_y\sqrt{1+t^2}} \left((1-s) \left(3u_{M, i_2} - 4u_{M-1, i_2-k} + u_{M-2, i_2-2k} \right) \right. \\ \left. + s \left(3u_{M, i_2} - 4u_{M-1, i_2-(k+1)} + u_{M-2, i_2-2(k+1)} \right) \right) = f_{M, i_2};$$

$$i_1 = 1, 2, \dots, M-1, \quad i_2 = 1, 2, \dots, N, \quad M = 1/h_x = 1/(mh_y), \quad N = 1/h_y;$$

where $k + s = mt$, k is integer, $0 \leq s < 1$. The first differential approximation to the discretization (2.8) in the interior of the domain is

$$(2.10) \quad FDA \left(L^{(h_x, h_y)} \right) = \partial_\xi - h_y^2 \frac{s(1-s)(1-2s)}{12m\sqrt{1+t^2}} \partial_{yyy} + h_y^3 \frac{s(1-s)(1-3s+3s^2)}{8m\sqrt{1+t^2}} \partial_{yyy}.$$

The first differential approximation to the outflow boundary condition discretization (2.9) is given by

$$(2.11) \quad FDA \left(L^{(h_x, h_y)} \right) = \partial_\xi - h_y^2 \frac{s(1-s)(1-2s)}{3m\sqrt{1+t^2}} \partial_{yyy} + h_y^3 \frac{s(1-s)(1-3s+3s^2)}{4m\sqrt{1+t^2}} \partial_{yyy}.$$

Comparing the coarse-grid FDAs (2.10) and (2.11) with the target grid FDA (2.7) one can derive the final form of the coarse-grid operators on a grid with an aspect ratio m

$$(2.12) \quad L^{(h_x, h_y)} u_{i_1, i_2} \equiv \frac{1}{4mh_y\sqrt{1+t^2}} \left((1-s) \left(u_{i_1+1, i_2+k} + 3u_{i_1, i_2} - 5u_{i_1-1, i_2-k} + u_{i_1-2, i_2-2k} \right) \right. \\ \left. + s \left(u_{i_1+1, i_2+(k+1)} + 3u_{i_1, i_2} - 5u_{i_1-1, i_2-(k+1)} + u_{i_1-2, i_2-2(k+1)} \right) \right) \\ + \frac{A_3}{h_y} \left(u_{i_1, i_2+2} - 3u_{i_1, i_2+1} + 3u_{i_1, i_2-1} - u_{i_1, i_2-2} \right) \\ + \frac{A_4}{h_y} \left(u_{i_1, i_2+2} - 4u_{i_1, i_2+1} + 6u_{i_1, i_2} - 4u_{i_1, i_2-1} + u_{i_1, i_2-2} \right) = f_{i_1, i_2}; \\ L^{(h_x, h_y)} u_{M, i_2} \equiv \frac{1}{2mh_y\sqrt{1+t^2}} \left((1-s) \left(3u_{M, i_2} - 4u_{M-1, i_2-k} + u_{M-2, i_2-2k} \right) \right. \\ \left. + s \left(3u_{M, i_2} - 4u_{M-1, i_2-(k+1)} + u_{M-2, i_2-2(k+1)} \right) \right) \\ + \frac{\bar{A}_3}{h_y} \left(u_{i_1, i_2+2} - 3u_{i_1, i_2+1} + 3u_{i_1, i_2-1} - u_{i_1, i_2-2} \right) \\ + \frac{\bar{A}_4}{h_y} \left(u_{i_1, i_2+2} - 4u_{i_1, i_2+1} + 6u_{i_1, i_2} - 4u_{i_1, i_2-1} + u_{i_1, i_2-2} \right) = f_{M, i_2}; \\ i_1 = 1, 2, \dots, M-1, \quad i_2 = 1, 2, \dots, N, \quad M = 1/h_x = 1/(mh_y), \quad N = 1/h_y;$$

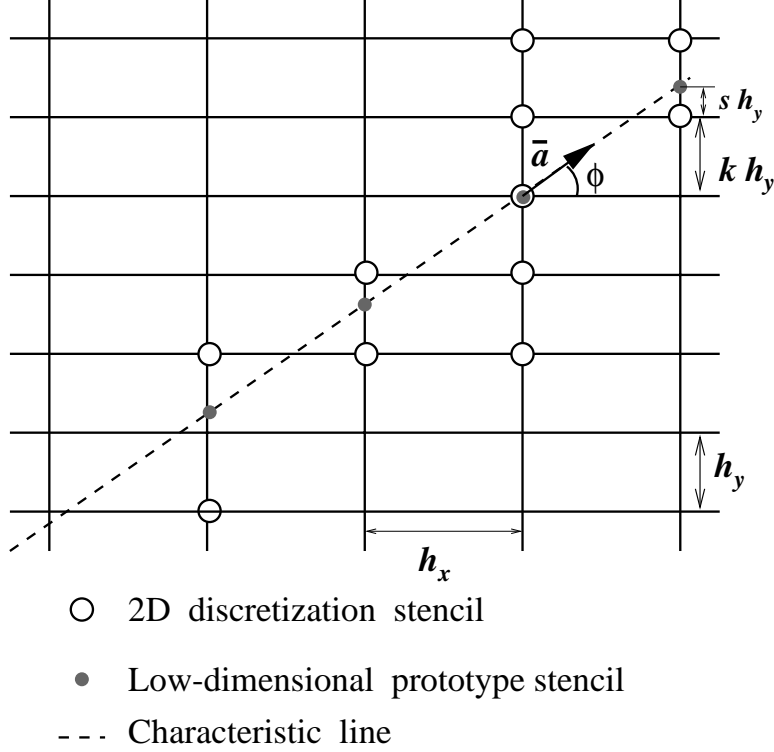


FIG. 2.1. 2D coarse-grid discretization stencil

where

$$\begin{aligned}
 (2.13) \quad A_3 &= \frac{1}{12\sqrt{1+t^2}} \left(-t(1-t)(1-2t) + s(1-s)(1-2s)/m \right); \\
 A_4 &= \frac{1}{8\sqrt{1+t^2}} \left(t(1-t)(1-3t+3t^2) - s(1-s)(1-3s+3s^2)/m \right); \\
 \bar{A}_3 &= \frac{1}{\sqrt{1+t^2}} \left(-t(1-t)(1-2t)/12 + s(1-s)(1-2s)/(3m) \right); \\
 \bar{A}_4 &= \frac{1}{\sqrt{1+t^2}} \left(t(1-t)(1-3t+3t^2)/8 - s(1-s)(1-3s+3s^2)/(4m) \right).
 \end{aligned}$$

See Figure 2.1 for a pictorial representation of the discretization stencil in the interior of the domain.

This choice of coarse-grid operator in combination with semicoarsening provides the same *absolute* p_h^H and *relative* \tilde{p}_h^H approximation orders of $L^{(h_x, h_y)}$ to L^h with respect to characteristic components, $p_h^H = \tilde{p}_h^H = 2$ (in terminology of [20]). This, in turn, ensures us a good coarse-grid correction to the characteristic error components.

Discretization (2.12) implies a small correction to the target-grid discretization of outflow boundary conditions. Generally speaking, the cross-characteristic interaction in discrete operators at the target-grid outflow boundary does not play an essential role since its influence on the solution in the interior is minimal. On coarse grids, however, where outflow boundary operators are “responsible” for a larger part of the domain, it is important to adjust their total cross-characteristic interaction to that interaction in the target-grid interior operator. We decided to apply the outflow boundary discretization proposed in (2.12) already on the target uniform grid ($m = 1$). It means that the target-grid outflow boundary discretizations include explicit terms with non-zero coefficients \bar{A}_3 and \bar{A}_4 . The values of A_3 and A_4 in the interior of the target grid are zeros by definition.

2.5. Strong Cross-Characteristic Coupling. Our multigrid construction employs semicoarsening and narrow coarse-grid discretization schemes supplied with explicit higher order terms (which are discrete approximations to the vertical derivatives of suitable orders) in order to maintain on the coarse grids the same cross-characteristic interaction as on the target (fine) grid. Then, the *characteristic error components* are well eliminated by the coarse-grid correction. The *noncharacteristic error components* must be reduced in relaxation. On several finest grids, where the direction of the strongest coupling approximately coincides with the characteristic direction, one can derive a pointwise relaxation scheme which reduces efficiently all the components oscillating in the characteristic direction. However, successive semicoarsening implies a fast decrease in the *inherent cross-characteristic interaction* on coarse grids and, hence, a fast increase in the weight of the explicit terms in the coarse-grid operators (since the total coarse-grid cross-characteristic interaction remains fixed). Thus, the direction of strongest coupling tends to be vertical. After several semicoarsening steps, hence, any pointwise relaxation scheme fails to reduce the noncharacteristic error components.

Roughly speaking, pointwise relaxation schemes lose their smoothing properties on grids where the “cross-characteristic” coupling becomes stronger than the “characteristic” one. The qualitative description of relations between the couplings can be derived from the analysis of the symbol of the corresponding coarse-grid operator (see Section 3.3.1). This analysis tells us that the efficiency of pointwise relaxations may degrade on grids with aspect ratios $m > 54$.

There are several ways to prevent this degradation:

1. The first is to use vertical *line relaxations* in which points located on the same vertical grid line are relaxed simultaneously. Such a relaxation is required only on coarse grids with aspect ratios $m > 54$. Practically it means that on fine grids ($m \leq 32$) a pointwise relaxation scheme can be efficiently used, while on coarser grids ($m \geq 64$) a line relaxation is employed. This method can be efficiently extended to the three dimensions (3D) (with a corresponding replacement of line relaxations with plane relaxations) and variable coefficient problems. This first method is extensively studied in this paper.
2. The second method is to widen gradually the basic narrow coarse-grid discretizations in order to increase the inherent cross-characteristic interaction and to reduce, in this way, the weight of the explicit terms in the coarse-grid discretization. This method is very flexible. It eliminates the need of using line relaxations on coarse grids and, therefore, it is well suited for multiblock grids required for calculations in complex geometries. This approach is briefly discussed in Section 6.
3. The third way is to use conditional coarsening technique, where a strong cross-characteristic coupling can be avoided by replacing part of the semicoarsening steps by full coarsening steps (see [11]). This conditional coarsening approach seems to be slightly cheaper than other in computing time but considerably more complicated to program, especially in extensions to variable coefficients.

3. Multigrid Cycles.

3.1. Multigrid Cycle for Low-Dimensional Prototype. The first necessary step is to derive an efficient solver for the prototype problem. This solver, then, will serve us as a model for a multigrid solver in the full dimension. The one-dimensional multilevel $V(\nu_1, \nu_2)$ cycle we have studied for the prototype problem consists of a colored relaxation scheme, an upwind-biased residual transfer and a linear interpolation of the coarse-grid correction. On each level, except the coarsest one where the problem is directly solved, ν_1 relaxation sweeps are performed before transferring residuals to the coarse grid and ν_2 sweeps are performed after receiving coarse-grid corrections. Below, we present a detailed description of all the components of this

cycle.

On the grid induced on the characteristic line, the one-dimensional prototype problem can be rewritten in new variables (cf. (2.4) and (2.5)) as

$$(3.1) \quad \begin{aligned} L^{(1D)}u_{i_1} &\equiv \frac{1}{4h_\xi} \left(u_{i_1+1} + 3u_{i_1} - 5u_{i_1-1} + u_{i_1-2} \right) = f_{i_1}, \\ i_1 &= 1, 2, \dots, N-1; \\ L^{(1D)}u_N &\equiv \frac{1}{2h_\xi} \left(3u_N - 4u_{N-1} + u_{N-2} \right) = f_N; \\ u_0 &= g_0, \quad u_{-1} = g_1; \end{aligned}$$

where h_ξ is the meshsize between nodes of the low-dimensional prototype discretization.

3.1.1. Relaxation Scheme. The downstream pointwise Gauss-Seidel relaxation scheme for the one-dimensional prototype interior equation (3.1) is unstable. In spite of the fact that an immediate error explosion can be prevented by using a color order of the relaxation passage, we decided to pick a stable relaxation scheme. This is done mainly because of the observation that (high-frequency) instabilities in schemes are usually accompanied with bad smoothing properties (especially, in further multidimensional extension). The relaxation scheme chosen for the problem (3.1) is a three-stage defect-correction-type scheme.

Stage 1: The residual function for the target problem (3.1) is computed.

$$(3.2) \quad r_{i_1} = f_{i_1} - L^{(1D)}\tilde{u}_{i_1}, \quad i_1 = 1, 2, \dots, N-1;$$

where \tilde{u}_{i_1} is the current solution approximation.

Stage 2: The correction v_{i_1} is calculated by *relaxing* the system

$$L_d v_{i_1} = r_{i_1}, \quad i_1 = 1, 2, \dots, N-1;$$

where v_{i_1} ($i_1 = -1, 0, \dots, N, N+1$) are initialized by zeros and operator L_d is the target operator $L^{(1D)}$ supplied with an additional (third order) dissipation term:

$$\begin{aligned} L_d v_{i_1} &\equiv \frac{1}{4h_\xi} \left(v_{i_1+1} + 3v_{i_1} - 5v_{i_1-1} + v_{i_1-2} \right) + \\ &\quad \frac{\lambda}{h_\xi} \left(v_{i_1+2} - 4v_{i_1+1} + 6v_{i_1} - 4v_{i_1-1} + v_{i_1-2} \right). \end{aligned}$$

The parameter λ is chosen to maintain stability in the downstream marching. In our tests, we have picked λ (approximately) equaled to the minimum positive value ensuring that all the (possibly complex) roots of the quadratic equation

$$\left(\frac{3}{4} + 6\lambda \right) x^2 - \left(\frac{5}{4} + 4\lambda \right) x + \left(\frac{1}{4} + \lambda \right) = 0$$

are inside the unit circle. It was found numerically, that $\lambda \approx 0.084$.

Stage 3: The current approximation \tilde{u}_{i_1} is corrected to the improved approximation \bar{u}_{i_1} by

$$\begin{aligned} \bar{u}_{i_1} &= \tilde{u}_{i_1} + v_{i_1}, \quad i_1 = 1, 2, \dots, N-1; \\ \bar{u}_N &= \frac{1}{3} \left(2f_N h_\xi - (-4\bar{u}_{N-1} + \bar{u}_{N-2}) \right). \end{aligned}$$

We still have some freedom in choosing the order of the relaxation passage on Stage 2. It is proved that the best smoothing is observed in the downstream marching. However, smoothing rates of colored

relaxation schemes are also quite good. A colored (with p colors) relaxation order is defined as following. One colored relaxation sweep consists of p passages, each passes through (approximately) N/p points. In the first passage, all the points with coordinates $i_1 = 1 + jp$ (j is a non-negative integer) are relaxed; in the second passage, all the points with coordinates $i_1 = 2 + jp$ are relaxed (in this passage the new values at previously relaxed points are used); and so on till all the points are updated. The minimum p required to enable a full parallelization and preclude the appearance of relaxation boundary layers is $p = 4$. This choice of p already provides a very good smoothing rate (see the 2D mode analysis in Section 3.3.2 where this 1D prototype appears as a particular case of alignment). Moreover, the soothing rates is further improved for $p > 4$. Thus, in practical problems the maximal possible p should be picked on. In our tests, we have mostly experimented with $p = 4$.

3.1.2. Residual Transfer. At this stage, we compute a coarse-grid approximation to the current fine-grid residual function (3.2). This fine-to-coarse transfer (restriction) is defined by

$$(3.3) \quad R_{i_1} = \frac{1}{2} \left(r_{2i_1} + r_{2i_1-1} \right),$$

where R and r denote the coarse- and fine-grid residual functions respectively.

3.1.3. Coarse-Grid Correction Interpolation. The coarse-grid correction V is interpolated (prolongated) to the fine grid by

$$(3.4) \quad \begin{cases} v_{2i_1} &= V_{i_1}, \\ v_{2i_1-1} &= \frac{1}{2} \left(V_{i_1-1} + V_{i_1} \right), \end{cases}$$

where v is the correction to the fine-grid solution approximation.

3.1.4. Efficiency. We have experimented with a two-level $V(0, 3)$ algorithm on different grids with different right-hand side functions f . The tests have demonstrated good convergence rates. The worst rate observed in a cycle during the solution process is about 3, while the asymptotic convergence rate is better than 6 per cycle. For $p = 8$ and the corresponding values are 3.7 (the worst per-cycle convergence rate) and 10 (the asymptotic convergence rate). The two-level discrete half-space and matrix analyses which are too cumbersome to be presented here (see some examples of the analyses in [8], [10], and [12]) predict the low bound for the convergence rates to be 2.3 per cycle. This bound does not depend on h and p providing $p \ll h^{-1}$.

3.2. Two-Level Cycles. In this section, we discuss the basic parts of the full-dimensional (2D) multi-grid cycle such as relaxation schemes, residual transfer and coarse-grid correction interpolation.

3.2.1. Pointwise and Line Relaxation Schemes. The relaxation schemes defined in this section are derived from the colored one-dimensional schemes described in Section 3.1.1. The operators involved are, of course, extended to the two dimensions. The target operator $L^{(h_x, h_y)}$ on an anisotropic grid with an aspect ratio m is given in (2.12). The “driver” operator L_d which is relaxed for the error equation on Stage 2 (see

Section 3.1.1), is defined as

$$\begin{aligned}
L_d^{(h_x, h_y)} v_{i_1, i_2} &\equiv L^{(h_x, h_y)} v_{i_1, i_2} \\
&+ \frac{\lambda}{h_\xi} \left((1-s) \left(v_{i_1+2, i_2+2k} - 4v_{i_1+1, i_2+k} + 6v_{i_1, i_2} - 4v_{i_1-1, i_2-k} + v_{i_1-2, i_2-2k} \right) \right. \\
&\quad \left. + s \left(v_{i_1+2, i_2+2(k+1)} - 4v_{i_1+1, i_2+(k+1)} \right. \right. \\
&\quad \left. \left. + 6v_{i_1, i_2} - 4v_{i_1-1, i_2-(k+1)} + v_{i_1-2, i_2-2(k+1)} \right) \right) \\
&- s(1-s) \left(1 - 3s + 3s^2 \right) \left(v_{i_1, i_2+2} - 4v_{i_1, i_2+1} + 6v_{i_1, i_2} - 4v_{i_1, i_2-1} + v_{i_1, i_2-2} \right),
\end{aligned}$$

where the nonalignment parameters k and s are defined in Section 2.4, $\lambda = 0.084$, $h_\xi = mh_y \sqrt{1+t^2}$, and the added artificial dissipation term approximates the differential operator $\lambda h_\xi^3 \partial_{\xi\xi\xi}$.

The number of colors p determines the order of relaxing the vertical grid lines. The lines with horizontal coordinates $i_1 = 1 + jp$, ($j \in \mathbb{Z}$) are relaxed first, then the lines with $i_1 = 2 + jp$, and so on; the lines to be relaxed last are those with $i_1 = (p-1) + jp$. In all the numerical tests below, we used $p = 4$. The difference between line and pointwise relaxation schemes to be used is how the solution values at the same vertical grid line are updated. In the line relaxation scheme, all the equations centered at the same vertical grid line are solved all together. Simultaneous replacement of solution values at all the grid nodes belonging to the line reduces residuals on this line to (nearly) zero. In a pointwise relaxation, the solution approximation is changed in a point to satisfy the only discrete equation defined at this point. The orders of relaxing the grid points on a line can be different. We use the four-color order in which relaxation on a line is performed in four passages. Each passage updates every fourth points. The first passage starts from the point with vertical coordinate $i_2 = 1$; the second, from the point with $i_2 = 3$; the third, from the point with $i_2 = 2$; and the last, from the point with $i_2 = 4$. This pointwise (sixteen-color) relaxation scheme is efficient and especially attractive for further implementations on parallel computers.

3.2.2. Intergrid Transfers. *The residual transfer* to the semicoarsened grid is given by

$$(3.5) \quad R_{i_1, i_2} = .5 \left(r_{2i_1, i_2} + (1-s)r_{2i_1-1, i_2-k} + sr_{2i_1-1, i_2-(k+1)} \right),$$

where $r_{i_1, i_2} = f_{i_1, i_2} - L^{(h_x, h_y)} u_{i_1, i_2}$ is the fine-grid residual function, and R_{i_1, i_2} is the coarse-grid residual function. This restriction operator possesses the *low-frequency order* $\bar{m}_R = 1$ and the *high-frequency order* $m_R = 1$ (see definitions of intergrid transfer orders in [20] and note that in semicoarsening algorithm only two fine-grid component are coupled on the coarse grid).

The coarse-grid correction operator is a linear interpolation defined by

$$(3.6) \quad \begin{cases} v_{2i_1, i_2} &= V_{i_1, i_2}, \\ v_{2i_1-1, i_2} &= \frac{1}{2} \left((1-s)V_{i_1-1, i_2-k} + sV_{i_1-1, i_2-(k+1)} + (1-s)V_{i_1, i_2+k} + sV_{i_1, i_2+(k+1)} \right), \end{cases}$$

where V is the coarse-grid solution and v is the correction to the fine-grid solution approximation. The low-frequency and the high-frequency orders of this prolongation operator are $\bar{m}_P = m_P = 2$.

Thus, the intergrid transfers satisfy the necessary conditions (derived in [20] and earlier in [4] and [13]) to provide a grid-independent convergence: $m_R + m_P > 1$ and $\max(\bar{m}_R, \bar{m}_P) > 0$.

3.2.3. Numerical Tests. In the full dimension, a two-level cycle $V_2(\nu_1, \nu_2)$ employing semicoarsening can be defined as the following six steps

- Step 1 *Prerelaxation sweeps*. The current approximation is improved by ν_1 relaxation sweeps.
- Step 2 *Residual transfer*. The coarse-grid approximation to the fine-grid residual function is calculated by means of (3.5).
- Step 3 *Coarse-grid operator*. The new values of the coarse-grid parameters m , k , s , A_3 , A_4 , \bar{A}_3 , and \bar{A}_4 are calculated. The coarse-grid equations (2.12) are formed.
- Step 4 *Coarse-grid solution*. The coarse-grid problem is solved. Its solution approximates the fine-grid error function. On this stage, we do not specify the solution method. It can be any method (direct or iterative) allowing to obtain an accurate solution to the coarse-grid problem.
- Step 5 *Coarse-grid correction*. The coarse-grid solution is interpolated by (3.6) to the fine grid. The current fine-grid approximation is corrected.
- Step 6 *Postrelaxation sweeps*. The current fine-grid approximation is improved by ν_2 relaxation sweeps.

We restricted ourselves to considering $V_2(0, 2)$ cycles. Such cycles (with $\nu_1 = 0$) are especially attractive for parallel computing (see [7]). In numerous computational tests, we compared the performance of $V_2(0, 2)$ cycles with either full or semicoarsening on grids with different aspect ratios $m = 1, 2, 4, \dots, 512, 1024$. Within the cycles employing semicoarsening, two types of relaxations (pointwise and line relaxations) were tested.

In all the two-level tests, we used the zero right-hand side function f_{i_1, i_2} . The inflow boundary conditions were chosen so that the function $U(x, y) = \sin(\omega(y - tx))$ is the exact continuous solution of the homogeneous problem (2.2), (2.3). The coefficients A_3 , A_4 , \bar{A}_3 , and \bar{A}_4 of the explicit terms in the fine-grid discretization were derived from the assumption that this fine grid itself was obtained from a uniform grid by ($\log_2 m$ steps of) semicoarsening. In other words, the total cross-characteristic interaction in the fine-grid discretization was the same as the inherent cross-characteristic interaction in the interior of a uniform grid with meshsize h_y .

A representative sample of the experimental results is shown on Figure 3.1. Each experiment included three different runs, each starting from the same initial approximation obtained by interpolation from the solution on semicoarsened grid. Both the pointwise and the line relaxation schemes used in the runs are described in Section 3.2.1 above. Run 1 (marked by pluses) employed the pointwise relaxation scheme and full coarsening. For small aspect ratios, where the inherent coarse-grid cross-characteristic interaction was stronger than the desired total cross-characteristic interaction, the coarse-grid values of A_3 , A_4 , \bar{A}_3 , and \bar{A}_4 were set to zero. Run 2 tested the pointwise relaxation scheme together with semicoarsening. Run 3 used the line relaxation scheme and semicoarsened coarse grid. Each run consisted of 20 cycles; the ratio of L_∞ norms of the residual before and after each cycle is calculated and pictured in the diagrams on Figure 3.1. In all the graphs on Figure 3.1, the horizontal coordinates serve to mark the cycle numbers. On vertical axes, the per-cycle convergence rates are displayed. Other notations used in titles on Figure 3.1 are following: $m = h_x/h_y$ is the fine-grid aspect ratio, where h_x and h_y are the corresponding x - and y -directional fine-grid meshsizes; t is the nonalignment parameter; ω is the frequency of the incoming component; RC is a relative coupling parameter. $RC > 1$ corresponds to discretizations for which smoothing properties of pointwise relaxations deteriorate. The methodology of calculation this RC parameter is described in Section 3.3.1. In all the tests pictured in Figure 3.1, we picked the nonalignment parameter $t = 0.2$, except the last test where $t = 0.98$. The value $t = 0.2$ roughly corresponds to the maximum inherent cross-characteristic interaction. The frequencies ω were chosen to satisfy to the two conditions: first, $\omega = 2^n\pi$, (n is integer) to reduce the total computational time exploiting the vertical periodicity; second, the fine-grid discrete solution should provide a reasonable accuracy in approximating the true solution of the differential equation. The last

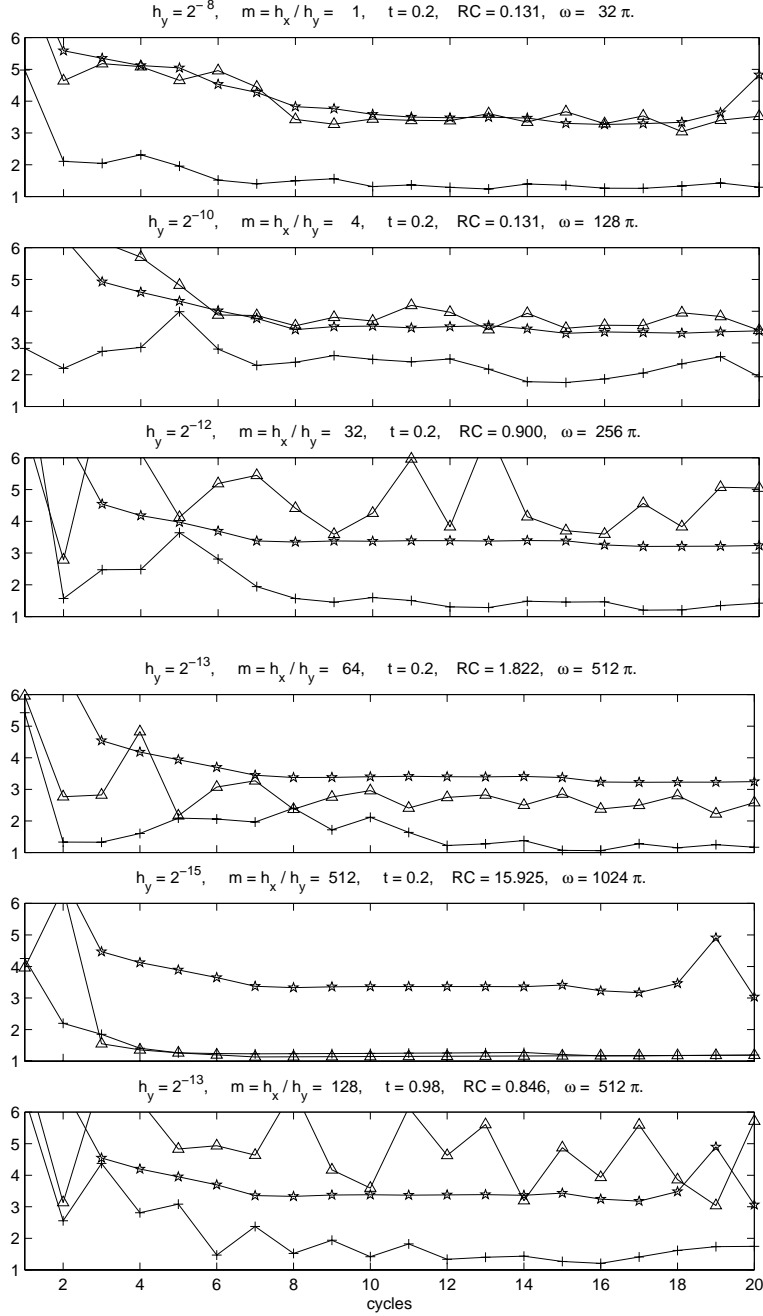


FIG. 3.1. Residual convergence history in two-level experiments: Run 1 (pluses) is $V_2(0, 2)$ cycle with full coarsening; Run 2 (triangles) is $V_2(0, 2)$ cycle with semicoarsening and pointwise relaxation; Run 3 (pentagrams) is $V_2(0, 2)$ cycle with semicoarsening and line relaxation.

experiment was added to confirm the claim that the algorithm efficiency, actually, depends on the relative coupling RC rather than on aspect ratios. (Compare the last experiment and the test on grid with $m = 32$). In particular, in cases of alignment ($t = 0$ or $t = 1$), the pointwise relaxation scheme can be efficiently applied on any grid with any aspect ratio.

The first very prominent observation from analyzing the results of numerical tests is the superiority of the semicoarsening algorithms over the algorithm with full coarsening. The two semicoarsening algorithms

show a similar behavior for discretizations with small values of the relative coupling ($RC \leq 1$, $m \leq 32$). When $RC \gg 1$, only the algorithm employing the line relaxation scheme demonstrates a fast convergence.

Note 1 Attempts to use higher order intergrid transfer operators result in some improvements in the full-coarsening algorithm, especially, on grids with $RC \approx 1$. However, this improved convergence still cannot compete with convergence rates demonstrated in the semicoarsening algorithm employing the line relaxation scheme.

Note 2 Inclusion of these higher order operators into semicoarsening algorithms deteriorates the convergence.

3.3. Fourier Mode Analysis.

3.3.1. Coupling Analysis. The coupling analysis presented in this section studies the discrete operator symbol $L(\bar{\theta})$, $\bar{\theta} = (\theta_x, \theta_y)$. By definition, the symbol of a discrete operator is the response of this operator on the discrete Fourier component $e^{i(\theta_x i_1 + \theta_y i_2)}$.

$$L^{(h_x, h_y)} e^{i(\theta_x i_1 + \theta_y i_2)} = L(\bar{\theta}) e^{i(\theta_x i_1 + \theta_y i_2)}.$$

The smoothing properties of pointwise relaxation schemes for discretized partial differential equations are essentially determined by the measure of h -ellipticity in the target discretization. (See [1] and [2].) Briefly, the measure μ of h -ellipticity is calculated as $\mu = \min |L(\bar{\theta})|$, where the minimum is taken over all the *high-frequency* Fourier components. The Fourier mode $e^{i(\theta_x i_1 + \theta_y i_2)}$ with normalized frequencies ($|\theta_x| \leq \pi$, $|\theta_y| \leq \pi$) is called a *high-frequency* mode if $\max(|\theta_x|, |\theta_y|) \geq \pi/2$. A discrete operator is called h -elliptic, if μ is separated from zero ($\mu \geq \text{constant} > 0$). Roughly speaking, the larger absolute values of the discrete operator symbol for given high-frequency Fourier components the better these components are eliminated by relaxation from the error function.

The multigrid construction proposed in Section 3.2 ensures a good approximation to the *characteristic* components of the solution. The *noncharacteristic* error components must be removed in relaxation. Let θ_ξ be a normalized characteristic frequency defined by $\theta_\xi + \pi = (\theta_x + m\theta_y) \bmod 2\pi$. The noncharacteristic components correspond to $|\theta_\xi| \geq \pi/2$. Thus, while the discretization is *semi h-elliptic* in the characteristic direction, i.e., $|L(\bar{\theta})|$ is large enough for all $\bar{\theta}$ satisfying $|\theta_\xi| \geq \pi/2$, one can derive a pointwise relaxation scheme which efficiently reduces the noncharacteristic error components. The measure of the *characteristic coupling* (see Section 2.5) can be computed as

$$\mu_0 = \min_{|\theta_\xi| \geq \pi/2} |L(\bar{\theta})|.$$

In our constant-coefficient model problem, the *cross-characteristic coupling* is mainly determined by the vertical interactions and, therefore, its measure can be defined as

$$\mu_1 = \min_{|\theta_y| \geq \pi/2} |L(\bar{\theta})|.$$

On grids with large aspect ratios $m > 64$ where $\mu_1 \gg \mu_0$, the discretization becomes semi h -elliptic in the vertical rather than in the characteristic direction and pointwise relaxation smoothing factors deteriorate for the noncharacteristic error components. Thus, the range of applicability of pointwise relaxations can be described by the value of the *relative coupling* parameter $RC = \mu_1/\mu_0$: if $RC \leq 1$, then one can derive an efficient pointwise smoother, otherwise, a line relaxation should be used. The RC values in different two-level tests are displayed on Figure 3.1.

3.3.2. Smoothing Factor of Four-Color Line Relaxation. The symbol of the four-color line relaxation $Z(\bar{\theta})$ defined in Section 3.2.1 is a 4-by-4 error amplification matrix acting on a four of Fourier modes $e^{i(\theta_x^j i_1 + \theta_y^j i_2)}$, $j = 0, 1, 2, 3$; where θ_x^j are normalized frequencies satisfying $\theta_x^j + \pi = (\theta_x + j\pi/4) \bmod 2\pi$ ($|\theta_x^j| \leq \pi$).

$$Z(\bar{\theta}) = \begin{pmatrix} C_0(\bar{\theta}^{(0)}) & C_1(\bar{\theta}^{(0)}) & C_2(\bar{\theta}^{(0)}) & C_3(\bar{\theta}^{(0)}) \\ C_3(\bar{\theta}^{(1)}) & C_0(\bar{\theta}^{(1)}) & C_1(\bar{\theta}^{(1)}) & C_2(\bar{\theta}^{(1)}) \\ C_2(\bar{\theta}^{(2)}) & C_3(\bar{\theta}^{(2)}) & C_0(\bar{\theta}^{(2)}) & C_1(\bar{\theta}^{(2)}) \\ C_1(\bar{\theta}^{(3)}) & C_2(\bar{\theta}^{(3)}) & C_3(\bar{\theta}^{(3)}) & C_0(\bar{\theta}^{(3)}) \end{pmatrix},$$

where $\bar{\theta}^j = (\theta_x^j, \theta_y)$. Parameters $C_0(\bar{\theta}), C_1(\bar{\theta}), C_2(\bar{\theta})$, and $C_3(\bar{\theta})$ are defined as

$$\begin{pmatrix} C_0(\bar{\theta}) \\ C_1(\bar{\theta}) \\ C_2(\bar{\theta}) \\ C_3(\bar{\theta}) \end{pmatrix} = M \left[\begin{pmatrix} 1 \\ 1 \\ 1 \\ 1 \end{pmatrix} - \begin{pmatrix} V_0(\bar{\theta}) \\ V_1(\bar{\theta}) \\ V_2(\bar{\theta}) \\ V_3(\bar{\theta}) \end{pmatrix} \right].$$

M is a constant matrix

$$M = \frac{1}{4} \begin{pmatrix} 1 & 1 & 1 & 1 \\ -i & -1 & i & 1 \\ -1 & 1 & -1 & 1 \\ i & -1 & -i & 1 \end{pmatrix}.$$

$$\begin{aligned} V_0(\bar{\theta}) &= L(\bar{\theta})/L_3(\theta_y), \\ V_1(\bar{\theta}) &= \left(L(\bar{\theta}) - e^{-i\theta_x} L_2(\theta_y) V_0(\bar{\theta}) \right) / L_3(\theta_y), \\ V_2(\bar{\theta}) &= \left(L(\bar{\theta}) - e^{-2i\theta_x} L_1(\theta_y) V_0(\bar{\theta}) - e^{-i\theta_x} L_2(\theta_y) V_1(\bar{\theta}) \right. \\ &\quad \left. - e^{2i\theta_x} L_5(\theta_y) V_0(\bar{\theta}) \right) / L_3(\theta_y), \\ V_3(\bar{\theta}) &= \left(L(\bar{\theta}) - e^{-2i\theta_x} L_1(\theta_y) V_1(\bar{\theta}) - e^{-i\theta_x} L_2(\theta_y) V_2(\bar{\theta}) \right. \\ &\quad \left. - e^{i\theta_x} L_4(\theta_y) V_0(\bar{\theta}) - e^{2i\theta_x} L_5(\theta_y) V_1(\bar{\theta}) \right) / L_3(\theta_y); \end{aligned}$$

$$\begin{aligned}
L_1(\theta_y) &= \left(\begin{aligned} &1/4 \left((1-s)e^{-i2k\theta_y} + se^{-i2(k+1)\theta_y} \right) \\ &+ \lambda \left((1-s)e^{-i2k\theta_y} + se^{-i2(k+1)\theta_y} \right) \end{aligned} \right) / (m\sqrt{1+t^2}), \\
L_2(\theta_y) &= \left(\begin{aligned} &-5/4 \left((1-s)e^{-ik\theta_y} + se^{-i(k+1)\theta_y} \right) \\ &-4\lambda \left((1-s)e^{-ik\theta_y} + se^{-i(k+1)\theta_y} \right) \end{aligned} \right) / (m\sqrt{1+t^2}), \\
L_3(\theta_y) &= \left(\begin{aligned} &3/4 + A_3 i \left(\sin(2\theta_y) - 2\sin(\theta_y) \right) + A_4 \left(2\cos(2\theta_y) - 8\cos(\theta_y) + 6 \right) \\ &+ \lambda \left(6 - s(1-s)(1-3s+3s^2)(2\cos(2\theta_y) - 8\cos(\theta_y) + 6) \right) \end{aligned} \right) / (m\sqrt{1+t^2}), \\
L_4(\theta_y) &= \left(\begin{aligned} &1/4 \left((1-s)e^{ik\theta_y} + se^{i(k+1)\theta_y} \right) \\ &-4\lambda \left((1-s)e^{ik\theta_y} + se^{i(k+1)\theta_y} \right) \end{aligned} \right) / (m\sqrt{1+t^2}), \\
L_5(\theta_y) &= \left(\begin{aligned} &\lambda \left((1-s)e^{i2k\theta_y} + se^{i2(k+1)\theta_y} \right) \end{aligned} \right) / (m\sqrt{1+t^2}).
\end{aligned}$$

t is the nonalignment parameter. $A_3, A_4, \lambda, k,$ and s are the parameters of discretization (2.12) on the grid with aspect ratio m . $L(\bar{\theta})$ is the discretization symbol:

$$L(\bar{\theta}) = e^{-i2\theta_x} L_1(\theta_y) + e^{-i\theta_x} L_2(\theta_y) + L_3(\theta_y) + e^{i\theta_x} L_4(\theta_y) + e^{i2\theta_x} L_5(\theta_y).$$

Following [16] we define the smoothing factor of the four-color line relaxation as the spectral radius of the matrix product $Q(\bar{\theta})Z(\bar{\theta})$, where

$$Q(\bar{\theta}) = \begin{pmatrix} q_0 & 0 & 0 & 0 \\ 0 & q_1 & 0 & 0 \\ 0 & 0 & q_2 & 0 \\ 0 & 0 & 0 & q_3 \end{pmatrix};$$

$q_j = 1$ ($j = 0, 1, 2, 3$), if $\pi/2 \leq |\theta_\xi^{(j)}| \leq \pi$, where $\theta_\xi^{(j)} + \pi = (\theta_x^{(j)} + mt\theta_y) \bmod 2\pi$; and $q_j = 0$ if $|\theta_\xi^{(j)}| < \pi/2$.

We picked $\lambda = 0.084$ and calculated smoothing factor Sm_1 for a variety of different slopes t and aspect ratios m (all other parameters are derived from these). In all cases, $Sm_1 < 0.54$. The smoothing rate of two successive four-color line relaxation sweeps Sm_2 which is defined as the spectral radius of $Q(\bar{\theta})Z(\bar{\theta})^2$ is $Sm_2 < 0.45$.

3.4. Multilevel Cycles. We performed many experiments with a *multilevel* $V(0, 2)$ cycle on uniform grids varying the nonalignment parameter t , the frequency ω of the incoming Fourier component, and the right-hand side function f . The multilevel cycle $V_d(\nu_1, \nu_2)$, where d is the cycle depth is defined similar to the two-level cycle (see Section 3.2.3) but Step 4 is replaced with recursive call of the same cycle applied to the coarse-grid problem. The coarsest grid where the problem is solved precisely is always the grid having

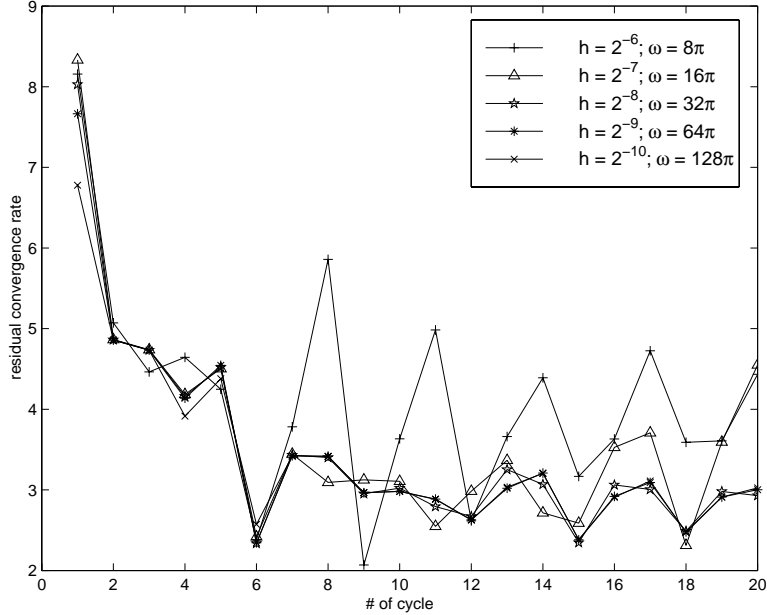


FIG. 3.2. Residual convergence history in multilevel experiments on target uniform (square) grids.

eight mesh spaces in the x direction in the interior part of the domain. We simplified the criterion of switching from pointwise to line relaxation to the following rule: pointwise relaxation sweeps are employed on grids with aspect ratios $m \leq 32$; on grids with higher aspect ratios the line relaxation is used. Figure 3.2 demonstrates results of numerical tests performed on different uniform target grids. Similar to the two-level tests we considered the homogeneous problem with boundary conditions derived from the assumption that function $U(x, y) = \sin(\omega(y - tx))$ is the exact solution of the differential problem. Initial approximations were obtained by interpolation of the exact discrete solution from the next immediate coarse grid with aspect ratio $m = 2$. In all this experiments, we picked $t = 0.2$ and solved the problems for incoming components with the same normalized frequency $\omega h = \pi/8$. The graphical results confirm that the multigrid cycle convergence rates are grid independent. The residual convergence rate histories on the three finest of the tested grids are practically undistinguished.

We also performed many numerical experiments testing the dependencies on the nonalignment parameter t and incoming frequencies ω . The results can be summarized as following:

1. In the first cycle, the L_∞ residual norm of the error is reduced by almost an order of magnitude.
2. In the first three cycles, the overall error reduction (also in the L_∞ residual norm) is more than two orders of magnitude.
3. The convergence rates in further cycles are ranged between 2 and 3.6 per cycle.

4. Full Multigrid Algorithm (FMG). The goal of an FMG algorithm can be formulated as fast obtaining an accurate solution for a *given discretization* on a *given target grid*. A solution approximation is considered to be accurate if its algebraic error is less than the discretization error. In this section, we present an FMG algorithm based on the multilevel $V(0, 2)$ cycle. The *setup* work required for this algorithm can be described as the following four steps:

Step 1. Target-grid problem. The discrete problem (2.12) is formulated on a uniform ($m = 1$) target grid.

The total cross-characteristic interaction for the entire algorithm is defined as the inherent cross-

characteristic interaction in the discretization in the interior of the target grid. Proper discretizations of the right-hand side function and the boundary condition functions are also performed. In our implementation, the corresponding discrete functions f_{i_1, i_2} , g_{i_2} and g'_{i_2} are formed by injection from their continuous counterparts.

Step 2. Next coarse grid. The next coarse grid is constructed by semicoarsening, where only meshsize in the reference x direction is doubled.

Step 3. Coarse-grid problem. The coarse-grid right-hand side function f^C is formed by the following averaging operator:

$$\begin{aligned} f_{i_1, i_2}^C &= 0.5f_{2i_1, i_2} + 0.25 \left[\begin{aligned} &(1-s) \left(f_{2i_1-1, i_2-k} + f_{2i_1+1, i_2+k} \right) \\ &+ s \left(f_{2i_1-1, i_2-(k+1)} + f_{2i_1+1, i_2+(k+1)} \right) \end{aligned} \right], \\ f_{M^C, i_2} &= 0.5 \left[f_{M, i_2} + (1-s) f_{M-1, i_2-k} + s f_{M-1, i_2-(k+1)} \right], \\ i_1 &= 1, 2, \dots, M^C - 1, \quad i_2 = 1, 2, \dots, N, \end{aligned}$$

where M^C and M ($M = 2M^C$) are parameters defining the number of mesh spaces in the x direction in the interior of the domain on the coarse and fine grids respectively. N is the number of mesh spaces in the y direction (the periodicity direction). In semicoarsening, N is the same on all the grids involved in calculations. The parameters k and s are the fine-grid nonalignment parameters ($k + s = mt$, k is integer, $0 \leq s < 1$, m is the fine-grid aspect ratio, $t = \tan \phi$ is the tangent of the nonalignment angle). The coarse-grid inflow boundary conditions are injected from the known true solution to the continuous problem. (See Note 1 below.) New values of coarse-grid discretization parameters such as the aspect ratio m^C , the nonalignment parameters k^C and s^C , the coefficients of the explicit cross-characteristic interaction terms in discretizations in the interior (A_3^C and A_4^C) and at the outflow boundary (\bar{A}_3^C and \bar{A}_4^C) are calculated.

Step 4. Recursion. The Steps 2 and 3 are repeated until the coarsest possible grid is reached and its problem is defined.

Note 1: Injecting true continuous solution values into the coarse-grid inflow boundary discretization is the easiest way to separate the issue of developing an efficient multigrid solver from the issue of deriving a proper high-order discretization to inflow boundary conditions. One possible solution for the latter is to use a central (or a downwind) discretization at the grid nodes adjacent to the inflow boundary. In this case, the coarse-grid inflow boundary conditions can be derived from those on the fine grid either by injection or by averaging.

The *execution* of the FMG algorithm involves the following four steps:

Step 1. Coarsest-grid solution. The problem on the coarsest grid is solved by some (direct or iterative) method.

Step 2. Initial fine-grid solution approximation. The initial approximation u on the currently fine grid is derived from the coarse-grid solution u^C by an interpolation which is the fourth order in the interior

of the domain (and the second order near the outflow boundary) in the characteristic direction.

$$\left\{ \begin{array}{l} u_{2i_1, i_2} = u_{i_1, i_2}^C, \\ u_{2i_1-1, i_2} = \frac{9}{16} \left[(1-s) \left(u_{i_1, i_2+k}^C + u_{i_1-1, i_2-k}^C \right) + s \left(u_{i_1, i_2+(k+1)}^C + u_{i_1-1, i_2-(k+1)}^C \right) \right] \\ \quad - \frac{1}{16} \left[(1-s) \left(u_{i_1+1, i_2+2k}^C + u_{i_1-2, i_2-2k}^C \right) + s \left(u_{i_1+1, i_2+2(k+1)}^C + u_{i_1-2, i_2-2(k+1)}^C \right) \right], \\ u_{M, i_2} = u_{M^C, i_2}^C, \\ u_{M-1, i_2} = \frac{1}{2} \left[(1-s) \left(u_{M^C, i_2+k}^C + u_{M^C-1, i_2-k}^C \right) + s \left(u_{M^C, i_2+(k+1)}^C + u_{M^C-1, i_2-(k+1)}^C \right) \right], \end{array} \right.$$

$$i_1 = 1, 2, \dots, M^C - 1, \quad i_2 = 1, 2, \dots, N.$$

Step 3. V Cycle. The obtained initial approximation is improved by one $V(0, 2)$ cycle.

Step 4. Recursion. Steps 2 and 3 are repeated until the target (finest) grid is reached. There one additional $V(0, 2)$ cycle is performed.

The total cost of this algorithm is about 30 *minimal work units*, where minimal work unit is defined as the number of computer operations required to evaluate residuals on the target grid. This work-unit count is about five times larger than usual in uniformly elliptic problems. It is contributed by (1) somewhat expensive relaxation schemes using defect-correction type iterations, (2) semicoarsening increasing the cost of coarse-grid calculations, and (3) the need to perform the second target-grid cycle. In fact, if the target discretization was changed to the discretization used in the correction step within relaxation (which has the same approximation order as our target discretization), then the cost of relaxation sweeps would be twice as cheap and, therefore, the total of the whole FMG algorithm would be reduced to 18 minimal work units.

In our numerical tests, we chose the right-hand side function f and the inflow boundary condition function g so that the function $U(x, y) = \sin(\theta_x x + \theta_y y)$ was the exact solution of the continuous problem (2.2), (2.3). The tests were performed with a six-level FMG algorithm solving the problem on a uniform target grid with $h_x = h_y = h = 2^{-8}$. We experimented with different values of parameters θ_x and θ_y . For each component, we checked five different characteristic inclinations $t = \tan \phi$. Some representative results are collected in Tables 4.1 and 4.2 where the target-grid discretization error is compared with the algebraic errors at three stages: immediately after obtaining the initial target-grid solution approximation and at the end of the first and the second improving target-grid cycles. In the tables, β_ξ is the characteristic frequency $\beta_\xi = \theta_x + t\theta_y$, and h_ξ is the characteristic meshsize $h_\xi = \sqrt{1+t^2}h$. A small absolute value of the normalized characteristic frequency $|\beta_\xi h_\xi| \approx 0$ indicates a characteristic component; when $0 \ll |\beta_\xi h_\xi| < \pi/2$, the characteristic oscillation frequency is intermediate; and $\pi/2 \leq |\beta_\xi h_\xi| \leq \pi$ characterizes a noncharacteristic solution component. The last column marked “No” shows the number of target-grid cycles (including those two from the FMG algorithm) required to get an approximation with the L_∞ norm of the residual error less than 10^{-10} .

Some conclusions derived from analyzing the numerical results are following.

1. For characteristic components, the target-grid algebraic error is already less than the discretization error on Step 2 (obtaining the initial target-grid solution approximation). This is due to the explicit terms introduced to all the coarse-grid discretizations. In this way, we obtain (nearly) the same characteristic component discretization errors on all the grids (the difference is proportional to h^4).
2. For components fast oscillating in the cross-characteristic direction, the algebraic error is *much better*

TABLE 4.1

Multigrid six-level FMG solver: characteristic and intermediate solution components.

t	$\beta_\xi h_\xi$	$\theta_y h$	$\theta_x h$	Discr. error	Algebraic error			No
					initial	1 cycle	2 cycle	
Characteristic components.								
0.1	0.000	0.393	-0.039	0.09572	0.01173	0.00176	0.00028	22
0.3	0.000	0.393	-0.118	0.11295	0.03494	0.00550	0.00099	22
0.5	0.000	0.393	-0.196	0.04570	0.06286	0.00718	0.00121	21
0.7	0.000	0.393	-0.275	0.11295	0.08332	0.01299	0.00229	22
0.9	0.000	0.393	-0.353	0.09572	0.10806	0.01584	0.00248	24
0.1	0.000	1.571	-0.157	0.99990	0.08726	0.02518	0.00618	21
0.3	0.000	1.571	-0.471	1.00006	0.12234	0.06842	0.01987	24
0.5	0.000	1.571	-0.785	0.99996	0.18733	0.13551	0.01981	23
0.7	0.000	1.571	-1.100	1.00006	0.12716	0.06039	0.01920	23
0.9	0.000	1.571	-1.414	0.99990	0.19453	0.01811	0.00537	21
Intermediate components.								
0.1	0.197	0.393	0.158	0.01842	0.11203	0.02097	0.00223	24
0.3	0.205	0.393	0.087	0.02952	0.10400	0.01697	0.00325	22
0.5	0.220	0.393	0.023	0.02903	0.09289	0.01502	0.00428	20
0.7	0.240	0.393	-0.035	0.02328	0.14294	0.02503	0.00389	22
0.9	0.264	0.393	-0.089	0.01640	0.15169	0.03876	0.00543	25
0.1	0.197	1.571	0.040	0.33494	0.21031	0.05228	0.00902	21
0.3	0.205	1.571	-0.266	0.54903	0.35938	0.06013	0.01651	23
0.5	0.220	1.571	-0.566	0.39790	0.42716	0.10210	0.02764	22
0.7	0.240	1.571	-0.860	0.24156	0.35623	0.10455	0.02441	23
0.9	0.264	1.571	-1.150	0.12979	0.27564	0.03267	0.00633	22
0.1	0.789	0.393	0.750	0.14177	1.07711	0.26069	0.07341	26
0.3	0.820	0.393	0.702	0.16808	1.43491	0.33600	0.08341	25
0.5	0.878	0.393	0.682	0.20206	1.67709	0.66490	0.09648	24
0.7	0.959	0.393	0.684	0.23211	2.15520	0.84395	0.19261	26
0.9	1.057	0.393	0.703	0.27629	1.81925	0.59167	0.26728	30
0.1	0.789	1.571	0.632	0.33086	0.76440	0.12903	0.02681	24
0.3	0.820	1.571	0.349	0.65990	0.93222	0.18361	0.03148	25
0.5	0.878	1.571	0.093	0.60069	1.09042	0.24374	0.04832	23
0.7	0.959	1.571	-0.141	0.51163	1.04272	0.25873	0.06088	24
0.9	1.057	1.571	-0.357	0.31980	1.35260	0.31203	0.04456	25

than the discretization one after the first improving target-grid cycle.

3. The second improving cycle is needed only for some components moderately oscillating in both the characteristic and cross-characteristic directions. On finer grids, these components are eventually transferred to the characteristic components. This justifies using FMG algorithm with only one V

TABLE 4.2
Multigrid six-level FMG solver: noncharacteristic solution components.

t	$\beta_\xi h_\xi$	$\theta_y h$	$\theta_x h$	Discr. error	Algebraic error			No
					initial	1 cycle	2 cycle	
Noncharacteristic components.								
0.1	1.579	0.393	1.539	0.76817	2.26395	0.98437	0.17369	28
0.3	1.640	0.393	1.522	0.87096	2.42296	1.14909	0.41368	26
0.5	1.756	0.393	1.560	1.04311	2.91390	1.88121	0.64483	26
0.7	1.917	0.393	1.643	1.31669	3.18658	1.67748	0.29945	27
0.9	2.113	0.393	1.760	1.70706	3.33678	1.97781	0.47206	29
0.1	1.579	1.571	1.422	0.85619	1.85721	0.38794	0.07397	24
0.3	1.640	1.571	1.169	1.07279	2.06405	0.40828	0.11672	25
0.5	1.756	1.571	0.971	1.53469	2.59033	0.96062	0.27004	24
0.7	1.917	1.571	0.818	1.59207	2.37166	0.76083	0.22509	25
0.9	2.113	1.571	0.700	1.59522	2.33271	0.75898	0.14614	27

cycle on coarse levels.

Note 2: In nonelliptic problems, there are some “pathological” noncharacteristic components which exhibit very small discretization errors. Noncharacteristic components usually possess relatively large discretization errors (compared with characteristic components). However, a very special choice of parameters (solution component U and angle of attack ϕ) can result in vanishing discretization errors. It is clear that in such special situations we cannot expect the algebraic error to be smaller than or comparable to the discretization error at any stage of the algorithm. In spite of the fact that the algorithm fails to reach the discretization accuracy for these components, the *total* (algebraic plus discretization) error in these exceptional cases is much smaller than in neighboring regular cases. Moreover, upon any reasonable perturbation the behavior becomes normal: the algebraic error after the two improving target-grid cycles is already substantially below the level of the discretization error. It is thus clear in any case that the statement that the algebraic error of the FMG solution is less than the discretization error will most likely hold in any *real* calculations (where mostly nonpathological components and angles of attack exist). A detailed analysis of this phenomenon (for another type of nonelliptic equations) can be found in [8].

5. Adaptive Multigrid Algorithm (AMA). In this section, we present an adaptive multigrid algorithm approximating the true solution of the differential problem with a relative accuracy ϵ defined in advance. The choice of the target grid is a part of the solution process. We restricted ourselves to considering only uniform target grids and the target-grid discretization ((2.12) for $m = 1$) is also unchanged. Thus, the only parameter to be controlled is the target-grid mesh spacing h . The algorithm starts on a very coarse grid where the problem is easy to solve and, then, proceeds to finer target grids. On each target grid, the FMG algorithm defined in Section 4 is performed to solve the problem. The AMA stops further calculations when the relative difference (in a required norm) between the solutions on the two currently finest target grids is less than ϵ . In our numerical experiments, the L_∞ norm of the difference between the solutions on the previous target grid and the (injected) current-target-grid solution was served as the stopping criterion.

Formally, the adaptive multigrid algorithm AMA-FMG employing the FMG cycle described in Section 4 can be defined in the following 3 steps.

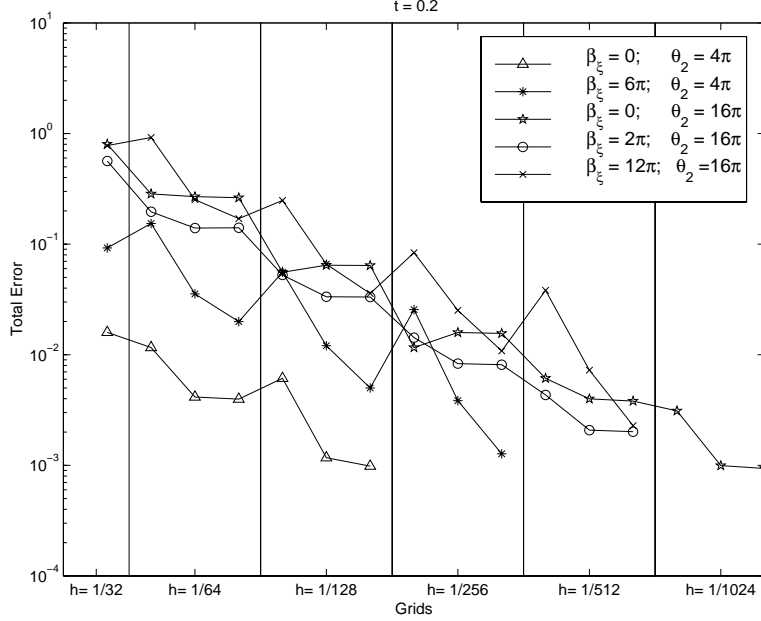


FIG. 5.1. *AMA – FMG:dependence on solution frequencies*

Step 1 Coarsest-grid solution. The problem on the coarsest grid is solved by some method.

Step 2 Solution on current target grid. Let u^{2h} be the solution on the previous target grid with meshsize $2h$. The current target grid is chosen to be the uniform grid with meshsize h . The FMG algorithm is employed to obtain the target-grid solution u^h .

Step 3 Comparison of the solutions. The solution u^h is restricted to the previous target grid by some fine-to-coarse intergrid transfer operator I_h^{2h} . In the simplest case, I_h^{2h} is the injection operator. The relative difference d_r is calculated as

$$d_r = \frac{\|u^{2h} - I_h^{2h} u^h\|}{\|u^{2h}\|}.$$

If $d_r < \epsilon$, then the solution on the current target grid is considered as final, otherwise algorithm proceeds to the next (finer) target grid (Step 2).

Figures 5.1 and 5.2 demonstrate the algorithm performance for different solution components and different angles of attack. In these experiments, the known true solution of the differential problem (2.2), (2.3) was $U(x, y) = \sin(\theta_1 x + \theta_2 y)$. The characteristic frequency β_ξ is calculated as $\beta_\xi = (\theta_1 + t\theta_2)/\sqrt{1+t^2}$. In all the tests shown on Figure 5.1, the nonalignment parameter t was set to $t = 0.2$ and the frequencies β_ξ and θ_2 were varied. We tested a large variety of frequencies. Figure 5.1 demonstrates just a representative sample of experiments. In the second set of experiments illustrated by Figure 5.2, the frequencies β_ξ and θ_2 were fixed but the angle of attack was changed. In all the tests, our goal was to obtain a 1%-accurate solution approximation u^h ($\epsilon = 0.01$), where the accuracy measured as the L_∞ norm of the relative total error ($\|U - u^h\|_\infty / \|U\|_\infty < \epsilon$). Recall, that the algorithm itself does not use the true solution at all. The decision whether to stop calculation or proceed to the next finer target grid is made by means of comparison of the *computed solutions* on the current and previous target grids. On the figures, the vertical coordinate marks (in the logarithmic scale) the total error of approximations obtained at different stages of the algorithm. The vertical lines separate the calculations performed on different target grids. The coarsest grid problem is solved by the FMG algorithm. The first value on each grid is the total error of the approximation obtained

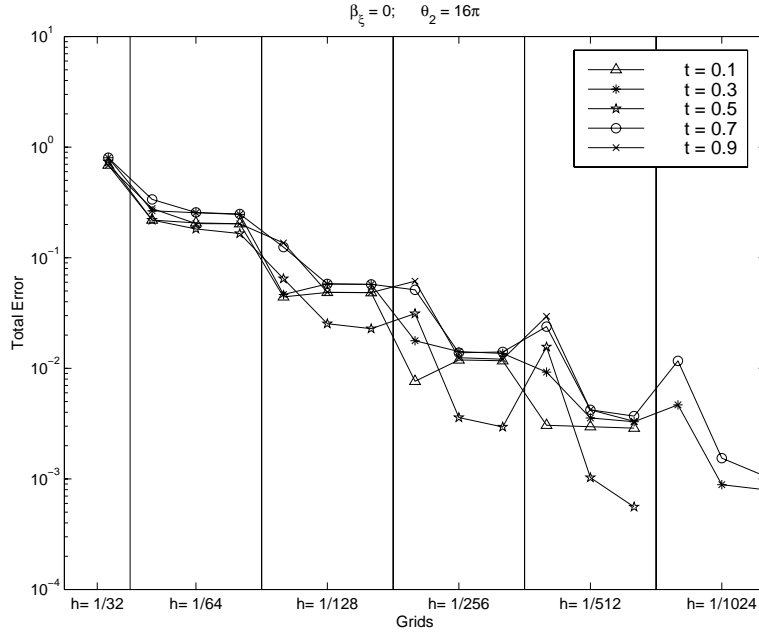


FIG. 5.2. AMA – FMG: dependence on angles of attack

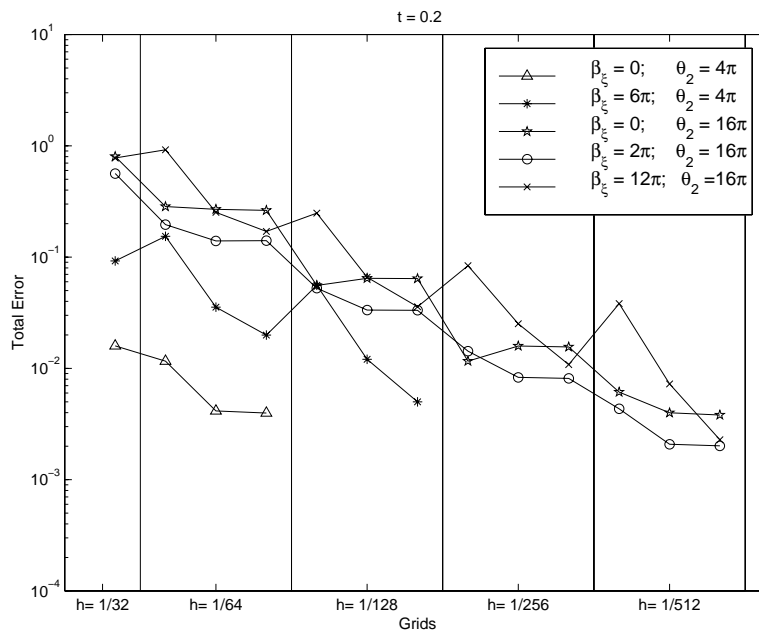


FIG. 5.3. AMA – FMG: 2ϵ tolerance

after the FMG solution interpolation (Step 2 in the FMG algorithm description in Section 4). The two following values are the total errors of the approximations obtained after the first and the second target-grid cycles respectively.

The demonstrated AMA performance is quite satisfactory. The total (relative) accuracy of final solutions is always *much better* than the desired 1%-accuracy. This overshooting is actually natural since in order to verify that the accuracy of the solution on a grid with meshsize h , the algorithm must compute the solution

on the next fine grid with meshsize $h/2$. We tried to change the tolerance of the algorithm weakening the stopping criterion to $d_r < D\epsilon$ ($D > 1$). We tested the same test-cases as in experiments traced on Figure 5.1. For $D = 2$, the algorithm sharply improved its efficiency (see Figure 5.3) finishing the calculations exactly on the grids where the required 1%-accuracy had been reached. Further increase of D results sometimes in final solutions with too large total errors.

6. Conclusions and Further Developments. The main difficulty appearing in solving nonelliptic equations by multigrid methods is a poor coarse-grid approximation to the characteristic error components. A novel approach proposed in this paper is based on the idea of using semicoarsening together with introduction of explicit terms into coarse-grid discretizations in order to maintain the same coarse-grid cross-characteristic interaction as on the target uniform grid. This construction allows us to get a good coarse-grid approximation to the characteristic components and in this way to solve the aforementioned problem.

Several multigrid algorithms were tested in this paper. All of them solve the two-dimensional constant-coefficient narrow second-order discretization of the convection equation on uniform Cartesian grids where the grid lines do not align with the characteristic direction. The following features of the tested multigrid algorithms were reported:

1. The algorithms used colored relaxation schemes on all the levels. It makes them very attractive for parallel computing.
2. The residual asymptotic convergence rate of the proposed $V(0,2)$ multigrid cycle is about 3 per cycle. This convergence rate far surpasses the theoretical limit $(4/3)$ predicted for standard multigrid algorithms using full coarsening. The reported efficiency does not deteriorate with increasing the cycle depth (number of levels) and/or refining the target-grid mesh spacing.
3. The full multigrid algorithm (FMG) using two $V(0,2)$ cycles on the target grid and just one $V(0,2)$ cycle on all the coarse grids always provides an approximate solution with the algebraic error less than the discretization error. The estimates of the total work in the FMG algorithm are between 18 and 30 minimal work units (depending on the target discretization). Thus, the overall efficiency of the FMG solver closely approaches (if does not achieve) the goal of the textbook multigrid efficiency.
4. A novel approach to deriving a discrete solution approximating the true continuous solution with a given relative accuracy is developed. An adaptive multigrid algorithm (AMA) using comparison of the solutions on two successive target grids to estimate the accuracy of the current target-grid solution is defined. This new criterion for the discrete approximation accuracy is much more effective and reliable than the residual monitoring widely used in practice. A desired relative accuracy ϵ ($0 < \epsilon \ll 1$) is accepted as an input parameter. The final target grid on which this accuracy can be achieved is chosen automatically in the solution process. The relative accuracy of the discrete solution approximation obtained by AMA is always better than the required ϵ -accuracy. The computational work required to compute this approximate solution is (nearly) optimal (comparable with the cost of the FMG algorithm applied to solve the problem on the optimally spaced target grid).

6.1. Extension to Three-Dimensional Problems. In 3D constant-coefficient case, the characteristics of the differential equation are still straight lines. Therefore, the low-dimensional prototype is essentially the same as (2.4)

$$(6.1) \quad \frac{1}{4h\sqrt{1+t_y^2+t_z^2}} \left(u_{i_1+1, i_2+t_y, i_3+t_z} + 3u_{i_1, i_2} - 5u_{i_1-1, i_2-t_y, i_3-t_z} + u_{i_1-2, i_2-2t_y, i_3-2t_z} \right) = f_{i_1, i_2, i_3},$$

where $t_y = \tan(\phi_y)$ is the tangent of the angle between the x -axis and the projection of the characteristic going through the grid node (i_1, i_2, i_3) onto the x - y coordinate plane; $t_z = \tan(\phi_z)$ is the same for the x - z coordinate plane. The ‘‘horizontal inclination assumption’’ is replaced in 3D with the x -axis inclination assumption: $|t_y| < 1$ and $|t_z| < 1$. Similar to 2D, the full dimensional discretization is derived from (6.1) by replacing values at the points with fractional indexes by (bilinear) interpolation from the values at genuine grid points placed in the same y - z grid plane. The second-order upwind discretizations are used at the outflow boundary. The multigrid solvers employ the semicoarsening procedure, where the only x -directional meshsize is doubled at each coarsening step. Explicit correcting terms introduced on coarse grids include discrete approximations to all possible third and fourth derivatives with respect to y and z . The coefficients of these terms are chosen from the condition that the first differential approximation to the coarse-grid discretization taken for the characteristic components is exactly the same as the characteristic-component FDA to the target-grid discretization. The 3D relaxation schemes used in the multigrid cycles are colored *plane* and *pointwise defect-correction-type schemes* where relaxation of a y - z plane (with given x -coordinate i_1) replaces the 2D vertical line relaxation wherever it is necessary. The coefficient λ of the additional stabilizing term which is the discretized fourth derivative with respect to the characteristic variable ξ is kept to be $\lambda = 0.084$. Note, that in plane relaxations, the precise solutions of planes are not required. The smoothing rate of a 3D plane relaxation scheme employing just one 2D V cycle to solve a plane problem is very much the same as the smoothing rate of a relaxation scheme solving plane problems to zero residuals. The intergrid transfers used in different multigrid algorithms are characteristic aligned and essentially repeat those in 2D: the restriction operators are upwind first order in V cycles and symmetric second order in FMG; the prolongation operators are symmetric second order in V cycles and symmetric fourth order in FMG. Preliminary experiments confirm that the efficiency of the proposed approach does not deteriorate in 3D.

6.2. Extension to Variable Coefficients. A generalization of the presented approach to *smooth nonrecirculating variable* velocity fields can be done in the way first tested in [6]. The cornerstone of this technique is a flexible recursive intergrid (fine-to-coarse) parameter transfer providing the target-grid accuracy in tracing the characteristic trajectories on coarse grids. In this way, we can construct an accurate basic coarse-grid discretization well aligned with the characteristic track. The cross-characteristic interaction in this discretization is again weaker than on the target grid and, therefore, we can supply it with explicit terms to get a good coarse-grid correction to the fine-grid characteristic error components. The main changes in discretizations to be obtained are coming from the lack of symmetry in the discrete low-dimensional prototype. It is still a one-dimensional four-point second-order discretization of the advection equation but on a *nonuniform* grid. The upwind-biased discretization corresponding to the Van Leer’s scheme with $\kappa = 0$ is the average of the second order central L^C and pure upwind L^U schemes:

$$\begin{aligned}
L u_{i_1, i_2} &\equiv \frac{1}{2} \left(L^C u_{i_1, i_2} + L^U u_{i_1, i_2} \right); \\
(6.2) \quad L^C u_{i_1, i_2} &\equiv \frac{1}{h_1 + h_2} \left[\frac{h_2}{h_1} u_{i_1+1, i_2+(k_1+s_1)} + \left(\frac{h_1}{h_2} - \frac{h_2}{h_1} \right) u_{i_1, i_2} - \frac{h_1}{h_2} u_{i_1-1, i_2+(k_2+s_2)} \right]; \\
L^U u_{i_1, i_2} &\equiv \frac{1}{h_3} \left[\left(\frac{h_2+h_3}{h_2} - \frac{h_2}{h_2+h_3} \right) u_{i_1, i_2} - \frac{h_2+h_3}{h_2} u_{i_1-1, i_2+(k_2+s_2)} + \frac{h_2}{h_2+h_3} u_{i_1-2, i_2+(k_3+s_3)} \right];
\end{aligned}$$

where h_1 , h_2 , and h_3 are distances between the discretization nodes of the low-dimensional prototype measured along the characteristic going through the grid point where the discrete operator is defined; k_1 , k_2 , and k_3 are integers denoting the vertical displacements (in meshsizes) from the point (i_1, i_2) ; s_1 , s_2 , and s_3 ($0 \leq s_1, s_2, s_3 < 1$) are the tuning parameters. (See Figure 6.1 for a pictorial explanation of the two-dimensional discretization stencil.) Generally speaking, this 2D scheme is second-order accurate only on those

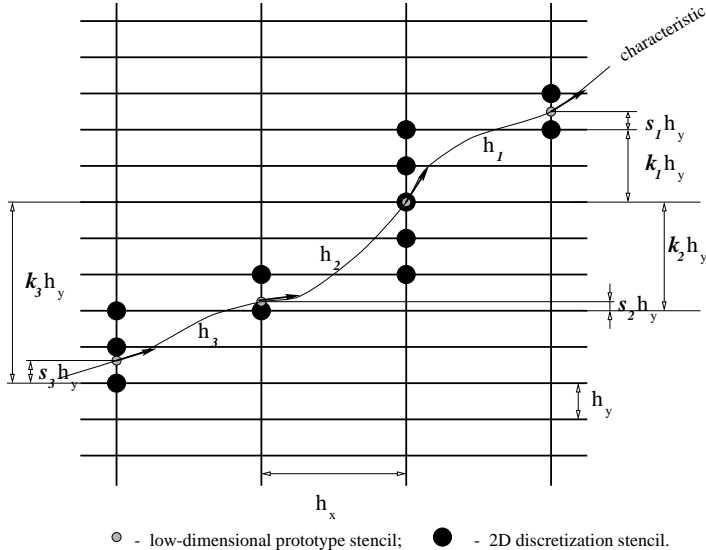


FIG. 6.1. *Coarse-grid discretization: variable velocity field.*

fine grids where the smoothness of velocity field can be exploit. The coefficients of the explicit terms are now calculated from the comparison of characteristic-component FDA coefficients of the true cross-characteristic derivatives (rather than the y -directional derivatives as in the constant-coefficient cases) because velocity directions may be different for different grid nodes (especially, on coarse grids). Preliminary numerical tests demonstrate a high efficiency of the approach in application to the variable-coefficient problems.

6.3. Avoiding Line Relaxations on Coarse Grids. If the characteristics of the differential equation change their general orientation over different parts of the domain, the entire domain should be divided into (possibly overlapped) subdomains (each occupying an $O(1)$ part of the domain and having a unique reference axis compatible throughout with the characteristic orientation) and the relaxation sweeps should be applied separately on each of the subdomains. In this view, using line relaxation schemes is undesirable because of possible lack of a global definition for lines. In many cases, this problem can be easily avoided since there is no need to solve simultaneously all the equation centered at the same vertical grid line. In other words, a block relaxation updating just a part of the line points at a time would be efficient as well. To keep the efficiency, the size of the overlap between neighboring blocks should be proportional to the relative coupling RC value (see Sections 3.2.3 and 3.3.1). This is one possible way to adjust the approach to a multiblock structure.

Another, even more efficient way is to widen the basic coarse-grid discretization on the grids (or even at separate grid nodes) where the value of the relative coupling is greater than (or comparable with) 1. The widening of discretization schemes is illustrated on Figure 6.2.

Widened discretization schemes possess stronger inherent cross-characteristic interaction and, therefore, the weight of the explicit terms in the total cross-characteristic interaction is reduced (RC is smaller). This technique is efficient only on grids with large enough RC , since the necessary condition to keep the efficiency is that the pointwise relaxation scheme is sensitive to the characteristic error components fast oscillating in the cross-characteristic direction. Combination of semicoarsening with widening discretization stencils allows us to keep RC bounded (around 1) and avoid in this way using line relaxation schemes making pointwise schemes always efficient.

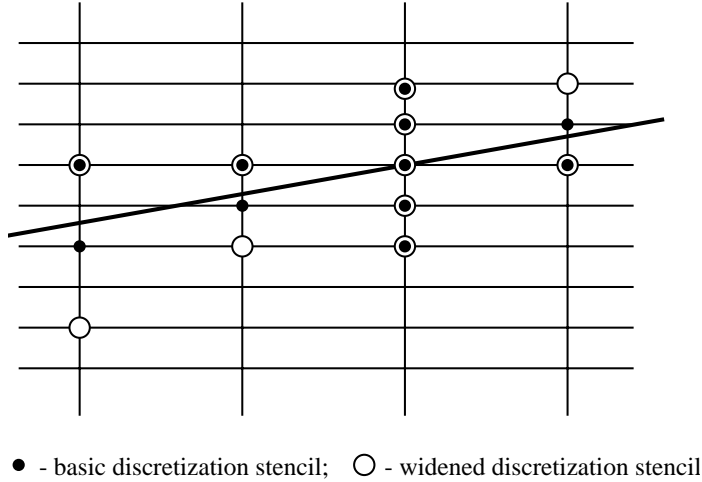


FIG. 6.2. *Coarse-grid discretization: widening discretization stencil.*

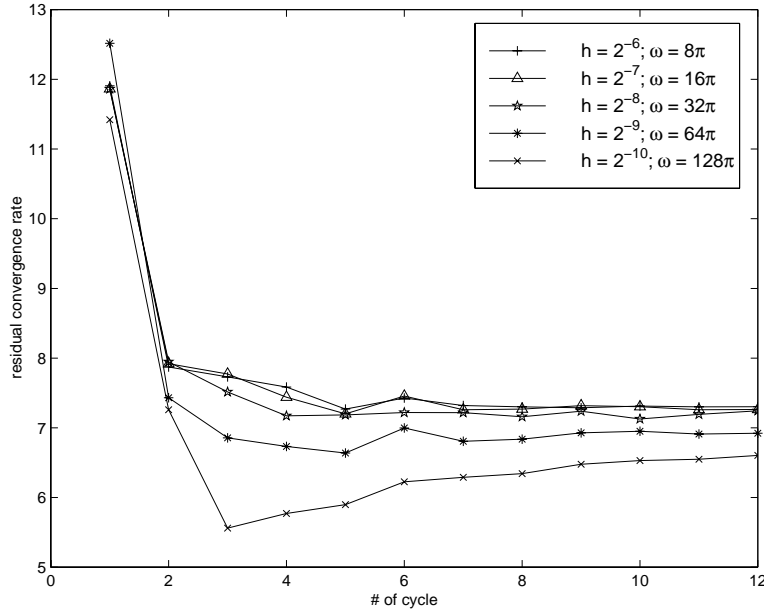


FIG. 6.3. *Residual convergence history in multilevel $V(0, 2)$ cycles employing the downstream relaxation. The target grids are uniform grids with meshsizes $h_x = h_y = h$. The problem is homogeneous ($f = 0$). ω is the frequency of the incoming oscillation. The nonalignment parameter $t = 0.2$.*

6.4. Note on Downstream Relaxation. The main subject of this paper is multigrid algorithms using colored relaxation schemes and, therefore, possessing a great parallelization potential. In this section, we remark about V cycles with line downstream (sequential order) relaxation schemes. We already mentioned that the efficiency of a colored relaxation scheme improves when more colors (in horizontal direction) are used. In this extend, the downstream relaxation is an extreme case where the number of colors coincides with the number of grid nodes in the x -direction. The downstream line relaxation demonstrates the best smoothing properties among other schemes. The smoothing factor Sm_d of this scheme is defined as

$$Sm_d(\bar{\theta}) = \max_{\pi/2 \leq |\theta_\xi| \leq \pi} \left[1 - \frac{L(\bar{\theta}) - (L_5(\theta_y)e^{i2\theta_x} + L_4(\theta_y)e^{i\theta_x})}{L_3(\theta_y) + L_2(\theta_y)e^{-i\theta_x} + L_1(\theta_y)e^{-i2\theta_x}} \right].$$

See all the definitions (for $\bar{\theta}$, θ_ξ , $L(\bar{\theta})$, $L_j(\theta_y)$, $j = 1, 2, 3, 4, 5$) in Section 3.3. The absolute value of $Sm_d(\bar{\theta})$ is always less than 0.4. Figure 6.3 shows excellent residual convergence rate histories of the $V(0, 2)$ cycle using the downstream line relaxation scheme. Different plots correspond to cycles starting on different uniform target grids.

REFERENCES

- [1] A. BRANDT, *Multigrid solvers for non-elliptic and singular-perturbation steady-state problems*. (unpublished). The Weizmann Institute of Science, Rehovot, Israel, December 1981.
- [2] ———, *Multigrid techniques: 1984 guide with applications to fluid dynamics*. Monograph (unpublished). GMD-Studie 85, GMD-FIT, Postfach 1240, D-5205, St. Augustin 1, Germany. Also available from Secretary, Department of Mathematics, University of Colorado at Denver, Colorado 80204-5300, 1985.
- [3] ———, *Rigorous local mode analysis of multigrid*, in Proc. 4-th Copper Mountain Conf. on Multigrid Methods, Copper Mountain, Colorado, April 1989.
- [4] ———, *Rigorous quantitative analysis of multigrid, I: Constant coefficients two-level cycle with L2-norm*, SIAM J. Num. Anal., 31 (1994), pp. 1695–1730.
- [5] ———, *Barriers to achieving textbook multigrid efficiency in CFD*, ICASE Interim Report 32, April 1998.
- [6] A. BRANDT AND B. DISKIN, *Multigrid solvers for nonaligned sonic flows*. Accepted for publication in SIAM J. Sci. Comp.
- [7] ———, *Multigrid solvers on decomposed domains*, in Domain Decomposition Methods in Science and Engineering, Y. A. K. A. Quarteroni, J. Periaux and O. Widlund, eds., Contemp. Math v. 157, Amer. Math. Soc., 1994, pp. 135–155.
- [8] ———, *Multigrid solvers for the non-aligned sonic flow: The constant coefficient case*, Computers and Fluids, 28 (1999), pp. 511–549. Also Gauss Center Report WI/GC-8 at The Weizmann Institute of Science, Israel, Oct. 1997.
- [9] A. BRANDT AND I. YAVNEH, *On multigrid solution of high-Reynolds incompressible entering flow*, J. Comput. Phys., 101 (1992), pp. 151–164.
- [10] J. A. DESIDERI AND P. W. HEMKER, *Convergence analysis of the defect-correction iteration for hyperbolic problems*, SIAM J. Sci. Comp., 16 (1995), pp. 88–118.
- [11] B. DISKIN, *Multigrid algorithm with conditional coarsening for the non-aligned sonic flow*, Electronic Trans. Num. An., 6 (1997), pp. 106–119.
- [12] B. DISKIN AND J. L. THOMAS, *Solving upwind-biased discretizations: Defect-correction iterations*, ICASE Report 99-14, March 1999.
- [13] P. W. HEMKER, *On the order of prolongations and restrictions in multigrid procedures*, J. Comput. Appl. Math., 32 (1990), pp. 423–429.
- [14] T. W. ROBERTS, D. SIDILKOVER, AND R. C. SWANSON, *Textbook multigrid efficiency for the steady Euler equations*, in 13th AIAA CFD meeting, 1996.
- [15] D. SIDILKOVER AND U. ASHER, *A multigrid solver for the steady-state Navier-Stokes equations using the pressure-Poisson formulation*, Matematica Aplicada e Computacional, 14 (1995), pp. 21–35.

- [16] K. STÜBEN AND U. TROTTENBERG, *Multigrid methods: Fundamental algorithms, model problem analysis and application*, in Multigrid Methods, W. Hackbusch and U. Trottenberg, eds., Lecture Notes in Math. 960, Springer-Verlag, Berlin, 1982, pp. 1–176.
- [17] S. TA'ASAN, *Canonical-variables multigrid method for steady-state Euler equations.*, in 14th International Conference on Numerical Methods in Fluid Dynamics, Deshpande and et al., eds., Proceedings Bangalore, Lecture Notes in Physics, India, 1994, Springer Verlag.
- [18] ———, *Essentially optimal multigrid method for steady state Euler equations*, AIAA Report 95-0209, 33rd Aerospace Sciences Meeting and Exhibit, January 1995.
- [19] N. YANENKO AND Y.I.SHOKIN, *Correctness of first differential approximations of difference schemes*, Dokl. Akad. Nauk SSSR, 182 (1968), pp. 776–778. (in Russian).
- [20] I. YAVNEH, *Coarse-grid correction for non-elliptic and singular perturbation problems*, SIAM J. Sci. Comput., 19 (1998), pp. 1682–1699.